

Artificial Photosynthetic System with Spatial Dual Reduction Site Enabling Enhanced Solar Hydrogen Production

Xiaowen Ruan, Depeng Meng, Chengxiang Huang, Minghua Xu, Dongxu Jiao, Hui Cheng, Yi Cui, Zhiyun Li, Kaikai Ba, Tengfeng Xie, Lei Zhang, Wei Zhang, Jing Leng, Shengye Jin, Sai Kishore Ravi,* Zhifeng Jiang,* Weitao Zheng,* Xiaoqiang Cui,* and Jiaguo Yu

Although S-scheme artificial photosynthesis shows promise for photocatalytic hydrogen production, traditional methods often overly concentrate on a single reduction site. This limitation results in inadequate redox capability and inefficient charge separation, which hampers the efficiency of the photocatalytic hydrogen evolution reaction. To overcome this limitation, a double S-scheme system is proposed that leverages dual reduction sites, thereby preserving energetic photo-electrons and holes to enhance apparent quantum efficiency. The design features a double S-scheme junction consisting of CdS nanospheres decorated with anatase TiO₂ nanoparticles coupled with graphitic C₃N₄. The as-prepared catalyst exhibits a hydrogen evolution rate of 26.84 mmol g⁻¹ h⁻¹ and an apparent quantum efficiency of 40.2% at 365 nm. This enhanced photocatalytic hydrogen evolution is ascribed to the efficient charge separation and transport induced by the double S-scheme. Both theoretical calculations and comprehensive spectroscopy tests (both *in situ* and *ex situ*) affirm the efficient charge transport across the catalyst interface. Moreover, substituting the reduction-type catalyst CdS with other similar sulfides like ZnIn₂S₄, ZnS, MoS₂ and In₂S₃ further confirms the feasibility of the proposed double S-scheme configuration. The findings provide a pathway to designing more effective double S-scheme artificial photosynthetic systems, opening up fresh perspectives in enhancing photocatalytic hydrogen evolution performance.

1. Introduction

Emulating natural photosynthesis has emerged as a promising avenue for renewable solar hydrogen production.^[1–6] While numerous material designs have been put forward for artificial photosynthesis, each comes with its set of challenges. Three key challenges to enhance the “solar-to-hydrogen” conversion efficiency are: selecting a photocatalyst with an appropriate bandgap, ensuring efficient carrier transport, and providing abundant active sites for surface redox reactions. Unfortunately, it is rare for a single photocatalyst to excel in all these aspects.^[7–12] In recent years, Z-scheme systems, which mimic natural photosystems, have been researched intensively for their potential in photocatalytic hydrogen evolution. These systems often employ suitable redox couples, such as all-solid-state and direct Z-schemes, to facilitate redox reactions.^[13–16] However, they tend to suffer from limitations like suboptimal bandgaps and rapid recombination of photogenerated carriers, resulting in less-than-ideal solar-to-hydrogen conversion

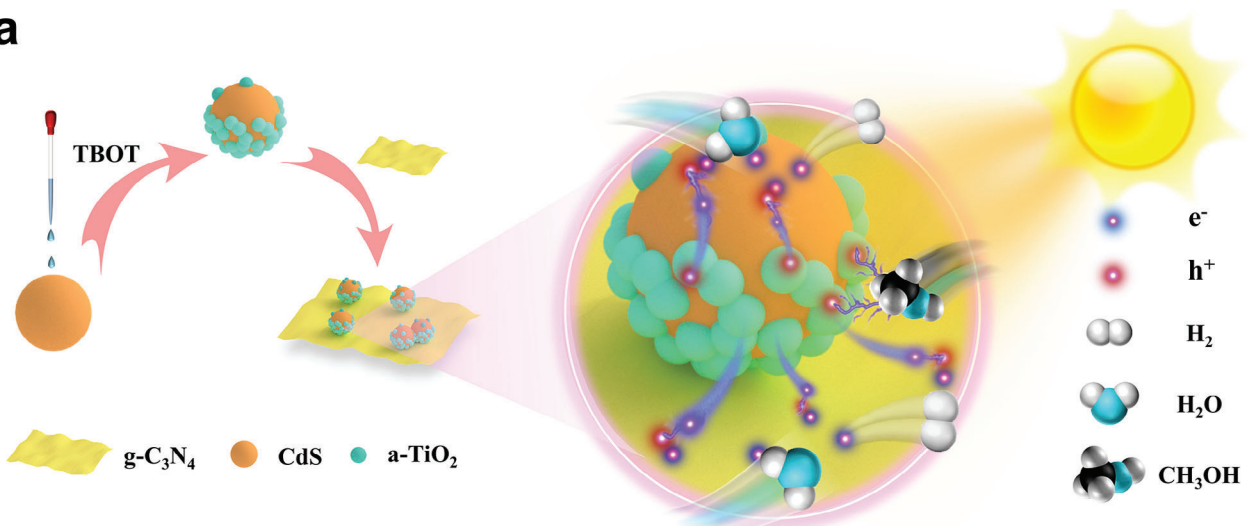
X. Ruan, D. Meng, C. Huang, M. Xu, D. Jiao, W. Zheng, X. Cui
 State Key Laboratory of Automotive Simulation and Control
 School of Materials Science and Engineering
 Key Laboratory of Automobile Materials of MOE
 Electron Microscopy Center
 Jilin University
 Changchun 130012, China
 E-mail: wtzhang@jlu.edu.cn; xqcui@jlu.edu.cn

X. Ruan, S. K. Ravi
 School of Energy and Environment
 City University of Hong Kong
 Tat Chee Avenue, Kowloon Hong Kong SAR
 E-mail: skravi@cityu.edu.hk
 H. Cheng, J. Leng, S. Jin
 State Key Laboratory of Molecular Reaction Dynamics
 Dalian Institute of Chemical Physics
 Chinese Academy of Sciences
 Dalian 116023, China

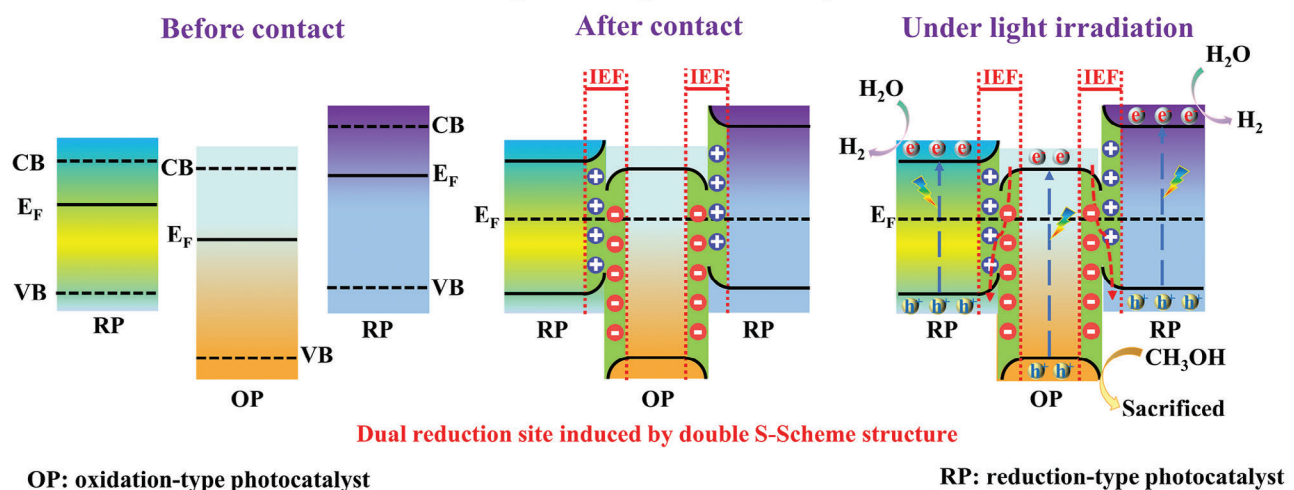
 The ORCID identification number(s) for the author(s) of this article can be found under <https://doi.org/10.1002/adma.202309199>

DOI: 10.1002/adma.202309199

Y. Cui, Z. Li
 Vacuum Interconnected Nanotech Workstation
 Suzhou Institute of Nano-Tech and Nano-Bionics
 Chinese Academy of Sciences
 Suzhou 215123, China
 K. Ba, T. Xie, L. Zhang
 College of Chemistry
 Jilin University
 2699 Qianjin Street, Changchun 130012, China
 Z. Jiang
 Institute for Energy Research
 Jiangsu University
 Zhenjiang 212013, P. R. China
 E-mail: jiangzf@ujs.edu.cn
 J. Yu
 Laboratory of Solar Fuel
 Faculty of Materials Science and Chemistry
 China University of Geosciences
 Wuhan 430074, P. R. China

a**b**

Artificial photosynthetic system



OP: oxidation-type photocatalyst

RP: reduction-type photocatalyst

Figure 1. Schematic diagram of heterojunction design and double S-scheme artificial photosynthetic system.

efficiency. To overcome these limitations, S-scheme (Step-scheme) heterojunctions have gained significant attention. Comprising both oxidative and reductive photocatalysts, these systems aim to enhance photocatalytic performance.^[17–20] Unlike traditional Z-scheme systems, S-schemes benefit from band bending, a strong internal electric field, and Coulombic attraction. These features collectively aid in charge separation and help sustain the system's photo-redox capabilities.

Although S-scheme photosystems offer many advantages, traditional single S-scheme junctions are limited by weak interphase interactions and poor integration between different catalyst phases.^[21–24] To address these challenges, various strategies have been explored, including the incorporation of a tri-phase catalyst into a single photosynthetic system.^[25–27] However, these efforts are hampered by unclear mechanisms for efficient carrier transfer and suboptimal catalyst interface interactions. Our group has previously introduced a “Twin S-scheme” architecture featuring a self-assembled structure (TSP) with graphitic carbon nitride nanosheets inserted between anatase and rutile

TiO_2 catalysts.^[18] The TSP catalyst shows robust interfacial interaction, a well-matched bandgap, and rapid carrier transport, thereby substantially improving photocatalytic hydrogen evolution performance.

Building on our prior research, we hypothesize that pairing two distinct reduction-type photocatalysts (RP) with an oxidation-type photocatalyst (OP) will improve interfacial interactions. Given that photocatalytic hydrogen production relies on electron-induced reduction reactions, having a surplus of electrons enhances the system's ability to convert solar energy into hydrogen. To this end, we introduce a double S-scheme artificial photosynthetic system with Dual Reduction Site Photocatalyst (DRSP), aimed at optimizing the charge separation and transport of photogenerated carriers while preserving their reductive potential (Figure 1a). Unlike our previous design, DRSP incorporates two RPs and one OP (Figure 1b). When these catalysts are in contact without light exposure, they generate dual internal electric fields (IEFs) and exhibit band bending (Figure 1b). Upon illumination, RP and OP regions become rich in electrons and holes,

respectively. The IETs ensure efficient spatial segregation of energetic photo-electrons and holes within the conduction band of RPs and the valence band of OP. This inhibits the undesired recombination of photogenerated charge carriers, thereby enhancing spatial carrier transport and maximizing redox capabilities. This new approach overcomes the limitations associated with traditional S-scheme, which have only a single reduction-active site.

Herein, we designed a double S-scheme structure with graphitic carbon nitride coupled by CdS nanospheres decorated with anatase TiO_2 nanoparticles (denoted as DRSP). This DRSP catalyst exhibited an impressive photocatalytic hydrogen evolution rate of $26.84 \text{ mmol g}^{-1} \text{ h}^{-1}$ and high apparent quantum efficiency of 40.2% under UV-vis illumination. Further investigations were conducted using various RPs (including ZnIn_2S_4 , ZnS , MoS_2 , and In_2S_3) paired with anatase TiO_2 and graphitic carbon nitride, all of which showed enhanced hydrogen production rates. Comprehensive theoretical calculations, *in situ*/ex situ characterizations, and band-structure analyses confirmed the charge transfer route of the double S-scheme configuration. Further supported by spectroscopic and photoelectrochemical tests, we confirmed the efficient separation and transfer of photogenerated carriers within this system. To the best of our knowledge, the apparent quantum efficiency achieved in this study is highly competitive when compared to previously reported TiO_2 -based photocatalysts. Our findings offer valuable insights for the design of future S-scheme photocatalysts with dual reduction sites, broadening the scope and potential of this approach.

2. Results and Discussion

The double S-scheme junction structure is probed using a transmission electron microscope (TEM). The junction consists of two-dimensional nanosheets ($\text{g-C}_3\text{N}_4$) and nanospheres (CdS) decorated with anatase nanoparticles (TiO_2) (Figure 2a). This structure aligns well with our anticipated design (Figure 2c). From the magnified views within the “Brown” and “Blue” rectangles, discernible space fringes of 0.316 and 0.352 nm were identified which correspond to CdS (101) and anatase TiO_2 (101), respectively (Figure 2b,d,e). This evidence affirms that the CdS nanospheres, anatase TiO_2 nanoparticles, and $\text{g-C}_3\text{N}_4$ nanosheets are in direct contact, establishing an active ternary heterojunction. So as to distinguish the three phases (CdS, anatase TiO_2 , and $\text{g-C}_3\text{N}_4$) in the ternary heterojunction, TEM images of pristine CdS, $\text{g-C}_3\text{N}_4$, and binary CdTi heterojunction are provided that further confirm the successful design and construction of DRSP heterojunction (Figures S1–S4, Supporting Information).

The structure of the DRSP catalyst is further characterized by fast Fourier transform (FFT) analysis (Figure 2f–g). This FFT calculated diagram represents the electron diffraction pattern, whose diffracted spot indexes have the same values as that of the Miller indices of the direct lattice planes of CdS and anatase TiO_2 , respectively. EDS-elemental mapping images show the elements of Cd, S, Ti, O, C, and N are uniformly dispersed on DRSP material, suggesting that the successful decoration of anatase TiO_2 nanoparticles on CdS nanospheres and well assembling on $\text{g-C}_3\text{N}_4$ nanosheets (Figure 2h; Figure S5 Supporting Information).

We can notice that the structure of CdS in XRD patterns is well maintained when decorated with anatase TiO_2 and assembled with $\text{g-C}_3\text{N}_4$ (Figure 2i and Figures S6 and S7 Supporting Information). Zeta potential tests demonstrate that the surface of CdS and anatase TiO_2 are positively charged while it in $\text{g-C}_3\text{N}_4$ is negatively charged (Figure 2j). This is why we first chose the hydrothermal method to prepare for binary CdTi catalyst and then assemble with $\text{g-C}_3\text{N}_4$ nanosheets through electrostatic interaction in our expected catalyst design system. In order to well understand the following proposed double S-scheme structure, we additionally investigate the loading position of Pt nanoparticles on binary TiO_2/CdS , $\text{CdS}/\text{g-C}_3\text{N}_4$, $\text{TiO}_2/\text{g-C}_3\text{N}_4$, and DRSP, respectively, further confirming the feasibility of double S-scheme structure (Figure S8 Supporting Information).

2.1. Component Analysis and Carrier Migration

The synthesized catalysts were further analyzed using X-ray photoelectron spectroscopy to examine the chemical states and elemental compositions (Figure S9, Supporting Information). As shown in Figure 3a, characteristic peaks at a binding energy of 404.9 and 411.4 eV are detected in the ex situ Cd 3d XPS spectra, ascribing to Cd^{2+} in pristine CdS.^[28] The binding energies of C 1s XPS spectra in $\text{g-C}_3\text{N}_4$ are located in 284.6 and 288.3 eV, which is ascribed to C–C and sp^2 -hybridized carbon, respectively (Figure 3b).^[29] The Ti 2p XPS (ex situ) of a- TiO_2 shows representative Ti 2p doublets of Ti^{4+} ions, similar to that of our previous work (Figure 3c).^[30] The binding energies of Cd 3d, S 2p, C 1s, and N 1s in DRSP have a shift toward higher energy levels in comparison to those of pristine CdS and $\text{g-C}_3\text{N}_4$, respectively, while the binding energy of Ti 2p in DRSP has a shift to lower energy level compared with pristine TiO_2 . Interestingly, compared with DRSP in the absence of light, the binding energies of Cd 3d, C 1s, S 3p, and N 1s under illumination have a shift toward lower energy levels while the binding energy of Ti 2p has a shift to higher energy level, suggesting the increased electron density (CdS and $\text{g-C}_3\text{N}_4$) and decreased electron density (TiO_2) (Figure 3a–c; Figure S10 Supporting Information). Meanwhile, we also characterize XPS spectra of DRSP catalyst after the light off and it can be noted that all the elements in the XPS spectra have returned to original binding energy position (Figure 3a–c). This reveals that an electron transfer can be generated through strong internal electric field at interfaces among the three phases in DRSP (CdS, TiO_2 and $\text{g-C}_3\text{N}_4$), which facilitates the construction of a dual reduction site induced by double S-scheme heterojunction.

The work function (Φ) is an important factor for investigating the interfacial charge transfer and double S-scheme mechanism of heterojunctions. According to the electrostatic potential, the energy difference between the vacuum and Fermi levels can be estimated. The theoretical work functions of CdS, $\text{g-C}_3\text{N}_4$, and TiO_2 are 5.78, 5.12, and 6.38 eV, respectively (Figure 3d–i). This means that CdS and $\text{g-C}_3\text{N}_4$ have a higher Fermi level than that of TiO_2 , revealing that the electrons will prefer to flow from CdS and $\text{g-C}_3\text{N}_4$ to TiO_2 after hybridization, which can then create an internal electric field among three phases and bend the energy bands of CdS, $\text{g-C}_3\text{N}_4$, and TiO_2 . This provides us with a solid foundation of double S-scheme transfer route mechanism. The

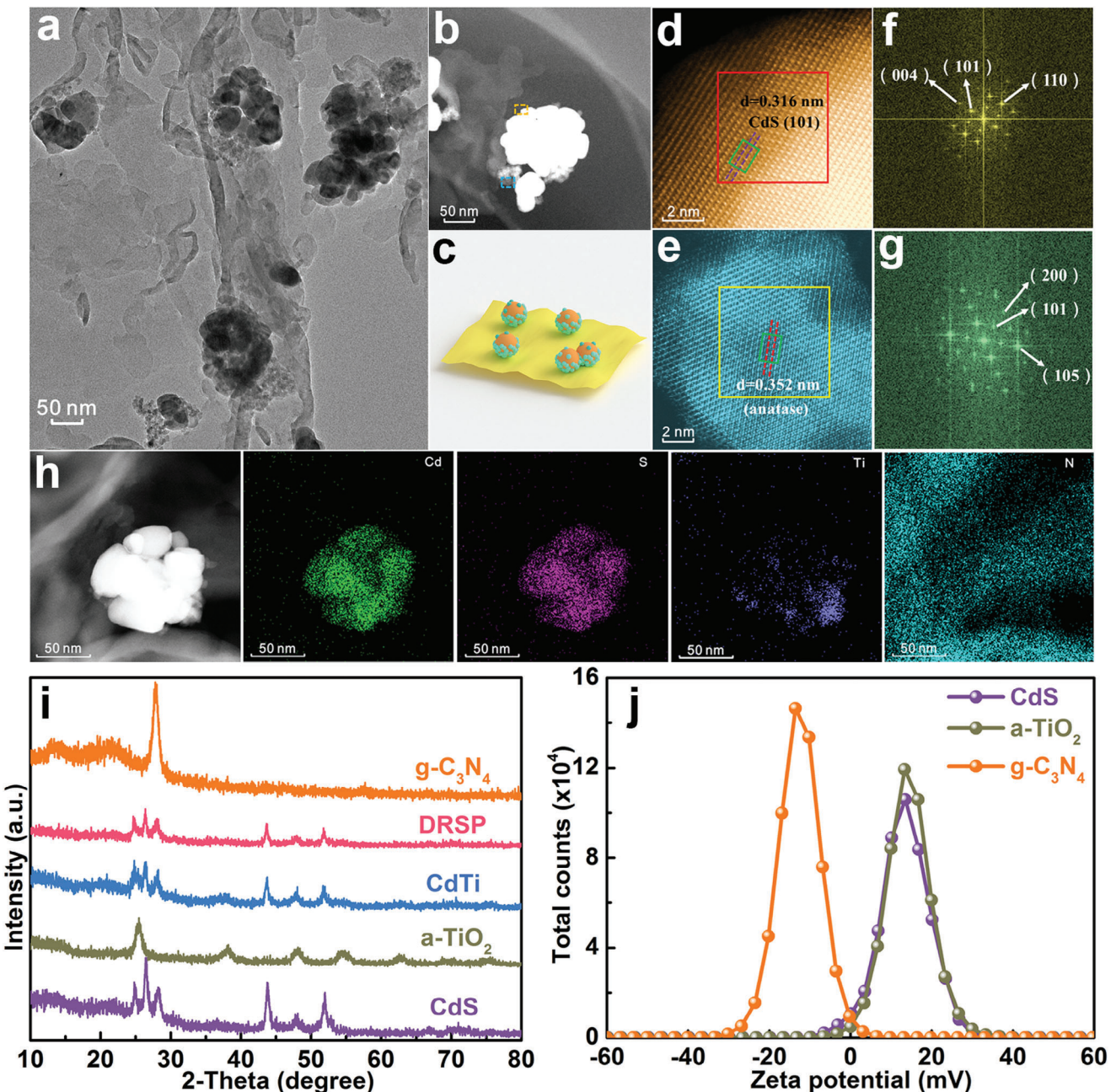


Figure 2. a) TEM and b) HAADF-STEM images of the DRSP heterojunction. c) Schematic illustration of DRSP junction composed of CdS nanospheres (orange), anatase titanium dioxide nanoparticles (green), and graphitic carbon nitride nanosheets (yellow). d,e) Enlarged images respectively of the brown and blue rectangles. f,g) FFT images obtained from the corresponding red square (CdS nanosphere) and yellow square (anatase TiO₂ nanoparticles), respectively. h) STEM elemental mapping of DRSP. i) XRD patterns of pristine g-C₃N₄, CdS, a-TiO₂, CdTi, and DRSP. j) Zeta potential of pristine CdS, a-TiO₂, and g-C₃N₄, respectively.

detailed double S-scheme mechanism is discussed in the following sections.

2.2. Carrier Mobility and Band Structure

Electron spin resonance (ESR) spin-trapping tests (both ex situ and in situ) are further conducted to investigate the charge sepa-

ration and transportation. As shown in Figure 4a,b, the canonical peaks of DMPO-·O₂ and DMPO-·OH are detected in as-prepared catalysts under light irradiation. Both DMPO-·O₂ and DMPO-·OH ESR signals are significantly enhanced in binary CdTi catalyst compared to pristine CdS and a-TiO₂, suggesting that the spatial distribution of reduction site (CdS part) and oxidation site (TiO₂ part) through a S-scheme charge transfer route. More importantly, for the heterojunction of DRSP, the

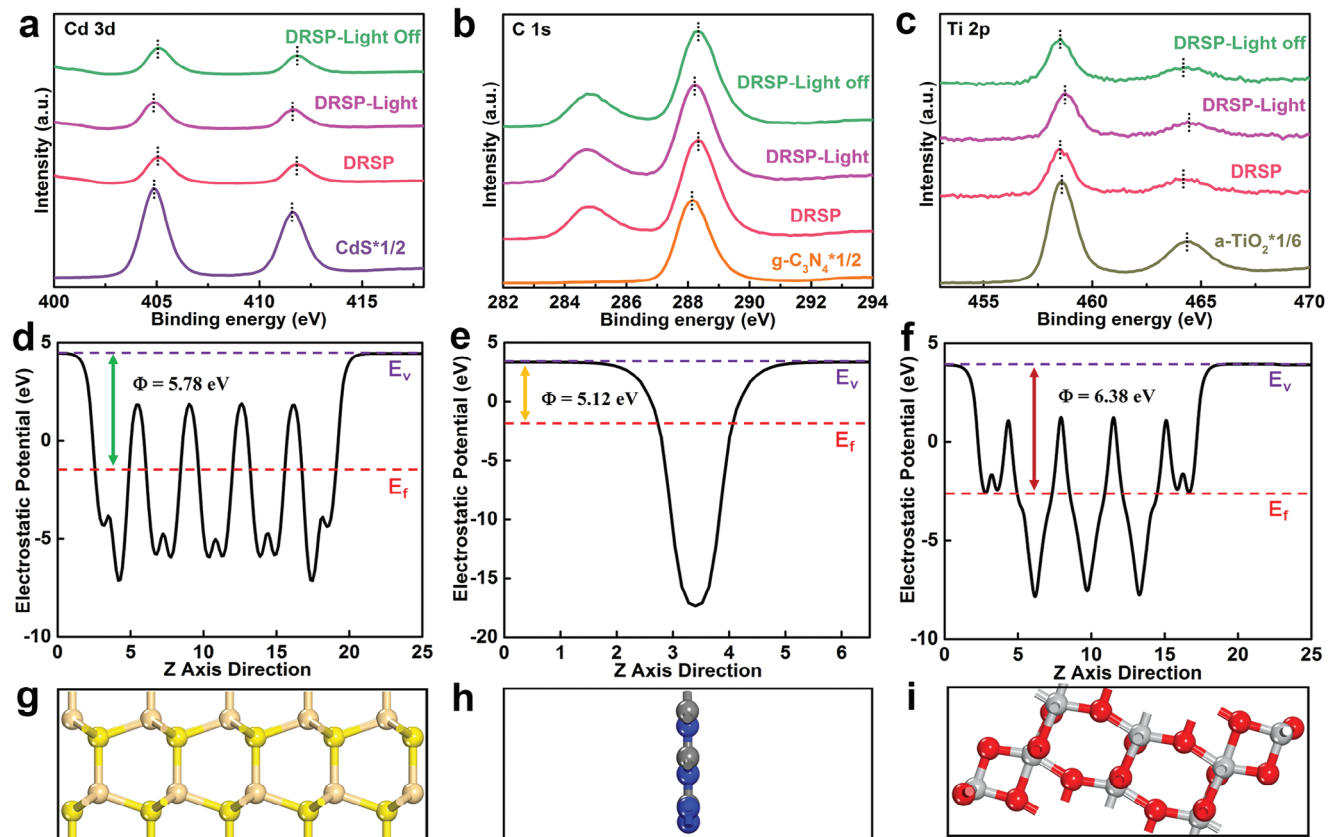


Figure 3. In situ and ex situ X-ray photoelectron spectroscopy spectra of a) Cd 3d, b) C 1s, and c) Ti 2p. The electrostatic potentials and corresponding models of d,g) CdS, e,h) g-C₃N₄, and f,i) a-TiO₂. The light pink, yellow, grey, blue, silver, and red spheres represent Cd, S, C, N, Ti, and O atoms, respectively. Purple and red dashed lines indicate the vacuum and Fermi energy levels.

ESR signals of DMPO-O₂⁻ and DMPO-OH are further significantly strengthened in comparison with those of CdS, a-TiO₂, g-C₃N₄ and CdTi, which confirms that DRSP catalyst has both reduction and oxidation ability for active species production, further demonstrating the dual reduction site induced by double S-scheme in DRSP. Meanwhile, no ESR signal peaks are observed both in DMPO-O₂⁻ and DMPO-OH under dark condition whereas typical ESR peaks became apparent under illumination (Figure 4c,d; Figures S11 and S12, Supporting Information). The peak intensity of two active radicals is gradually enhanced when the time of in situ irradiation is prolonged. This demonstrates that photogenerated carriers exhibit remarkable separation and transport efficiency through the double S-scheme, fostering the production of numerous active radical species. These findings provide substantial evidence supporting the superiority of the double S-scheme over the DRSP catalyst interface when exposed to light irradiation.

To investigate the optical properties and bandgap of the catalyst, UV/Vis diffuse reflectance spectra (UV/Vis DRS) and valence band XPS spectra (VB-XPS) are further tested. As shown in Figure 4e, the optical absorption edges of pristine CdS and g-C₃N₄ are within the visible light range. Pristine TiO₂ shows the optical absorption range from 350 to 450 nm while as-prepared DRSP shows an enhanced light absorption ranging from 500 to 600 nm, which is in favor of visible light absorption. The corre-

sponding intrinsic bandgaps of CdS, a-TiO₂, g-C₃N₄, and DRSP are 2.12, 3.20, 2.75, and 2.15 eV, respectively (Figure 4f). It can be noted that the narrowed bandgap of as-prepared DRSP catalyst is beneficial for the utilization of visible light. The estimated energy gaps between the valence band edge and the Fermi level versus RHE for C₃N₄, TiO₂, and CdS are 1.70, 2.85, and 1.72 eV, respectively (Figure 4g). Based on the bandgap and above theoretical work function, the band positions of C₃N₄, TiO₂, and CdS are proposed and the double S-scheme band structure is shown in Figure 4h according to the formula ($E_{CB} = E_{VB} - E_g$). When all the catalysts (C₃N₄, TiO₂, and CdS) contact each other, the electrons prefer to transfer from CdS and C₃N₄ to TiO₂, which can create two internal electric fields at three phases interfaces pointing from CdS and C₃N₄ to TiO₂ and bend the energy bands of CdS, C₃N₄, and TiO₂. When exposed to illumination, all the catalysts (C₃N₄, TiO₂, and CdS) are excited, generating photoelectrons and holes. Reduction-type photocatalysts of CdS and g-C₃N₄ form electron-rich area while oxidation-type photocatalysts of TiO₂ form hole-rich area. Under two internal electric fields (IET) and bent bands, the photogenerated holes on the valence band of CdS and g-C₃N₄ will be driven to simultaneously consume the photogenerated electrons on the conduction band of TiO₂. The electrons are accumulated on the conduction band of CdS and g-C₃N₄, respectively, while the abundant holes remain on the valence band of TiO₂, thus effectively promoting the

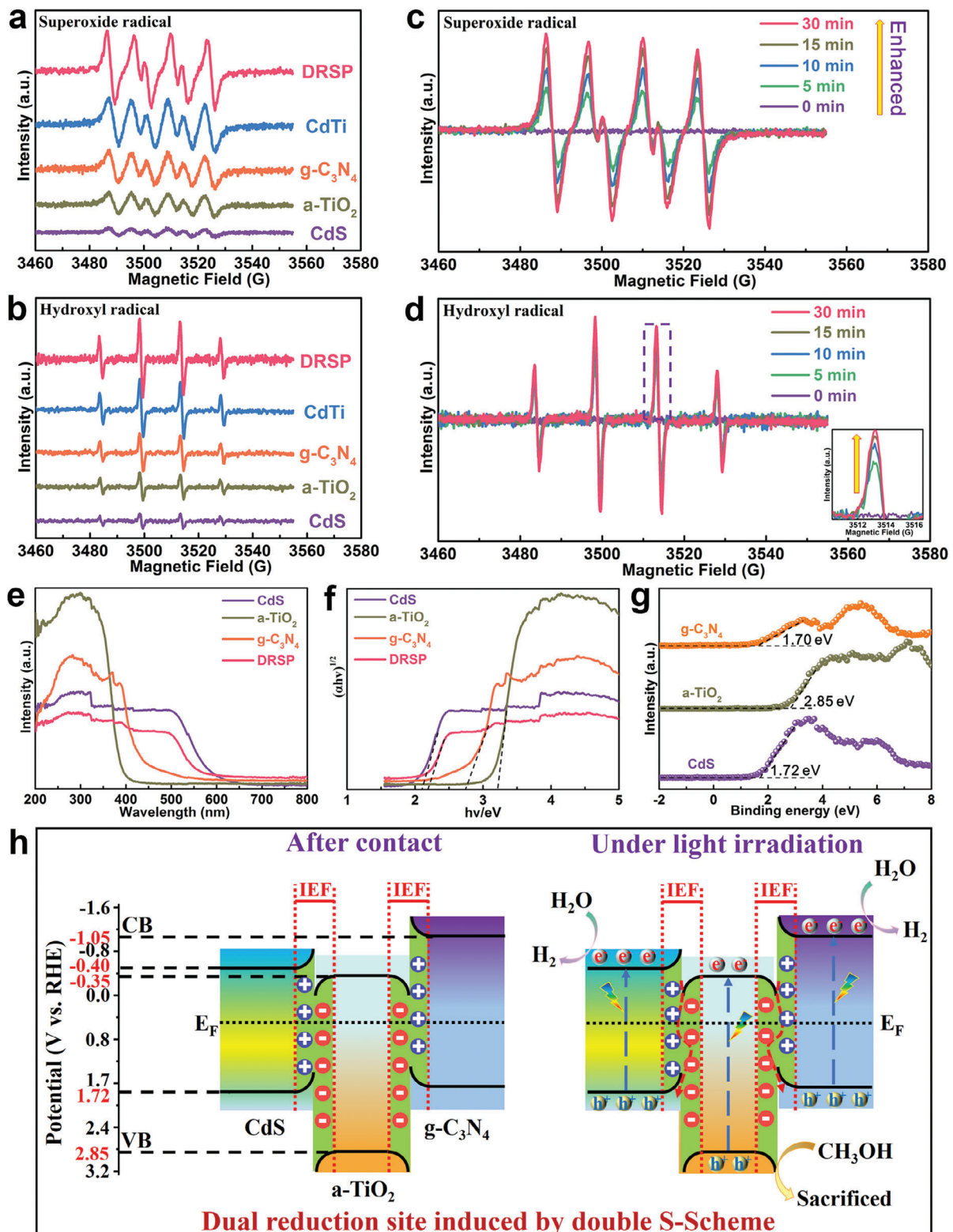


Figure 4. Electron spin-resonance spectroscopy (ESR) signals of CdS, a-TiO₂, g-C₃N₄, CdTi, and DRSP (a) in methanol dispersion for DMPO-superoxide radical and b) in aqueous dispersion for DMPO-hydroxyl radical under UV-vis light for 5 min, respectively. In situ ESR spectra of DRSP (c) in methanol dispersion and (d) aqueous dispersion under dark condition (purple line) and 5, 10, 15, and 30 min of light irradiation, respectively. e) UV-visible DRS of CdS, a-TiO₂, g-C₃N₄ and DRSP. f) Corresponding Tauc plots for CdS, a-TiO₂, g-C₃N₄ and DRSP using $(F(R)/hv)^{1/2}$ (Kubelka-Munk parameter) as a function of the photon energy. g) VB-XPS spectra of CdS, a-TiO₂, and g-C₃N₄. h) Band alignments for dual reduction site induced by double S-scheme heterojunction.

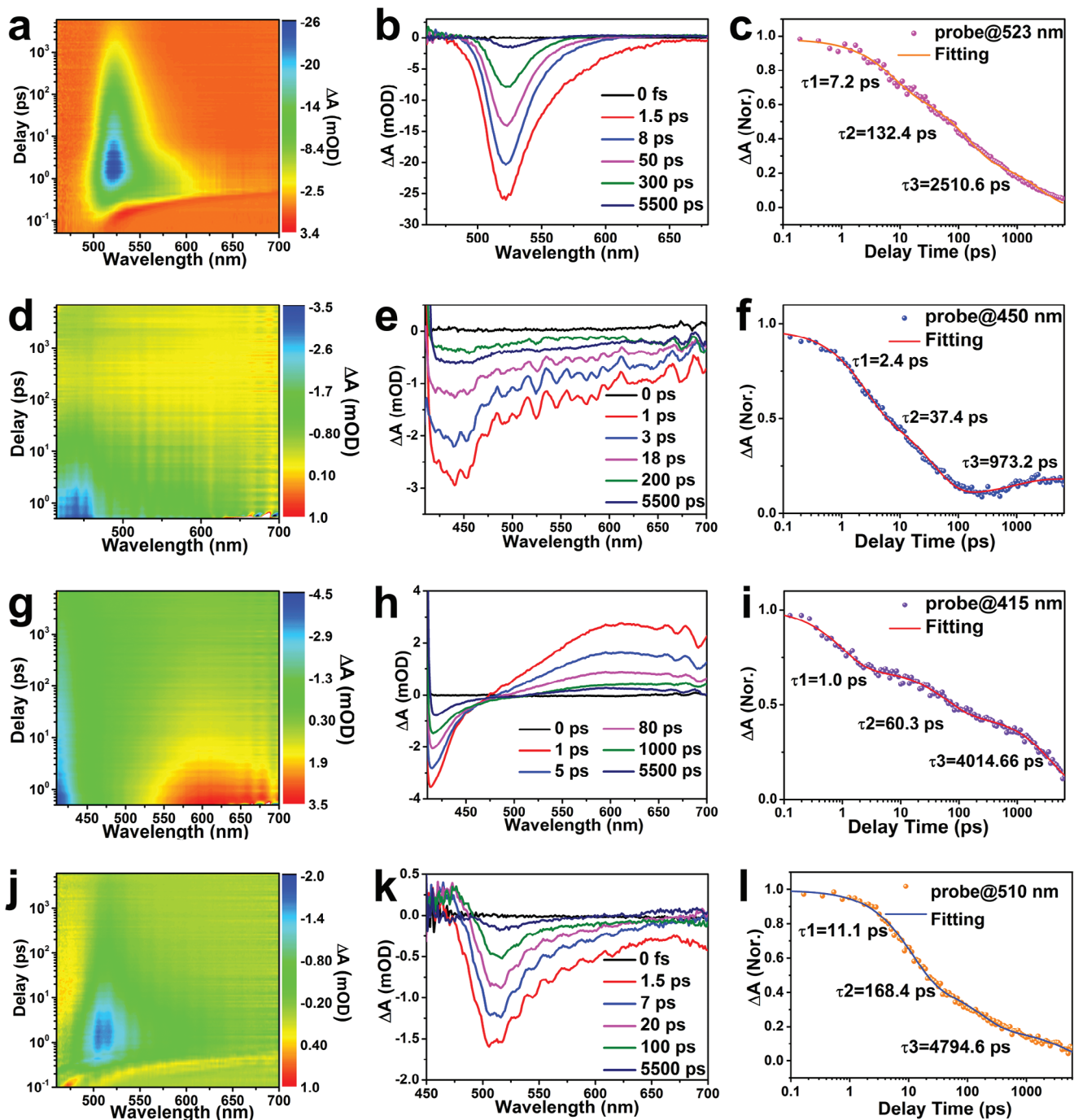


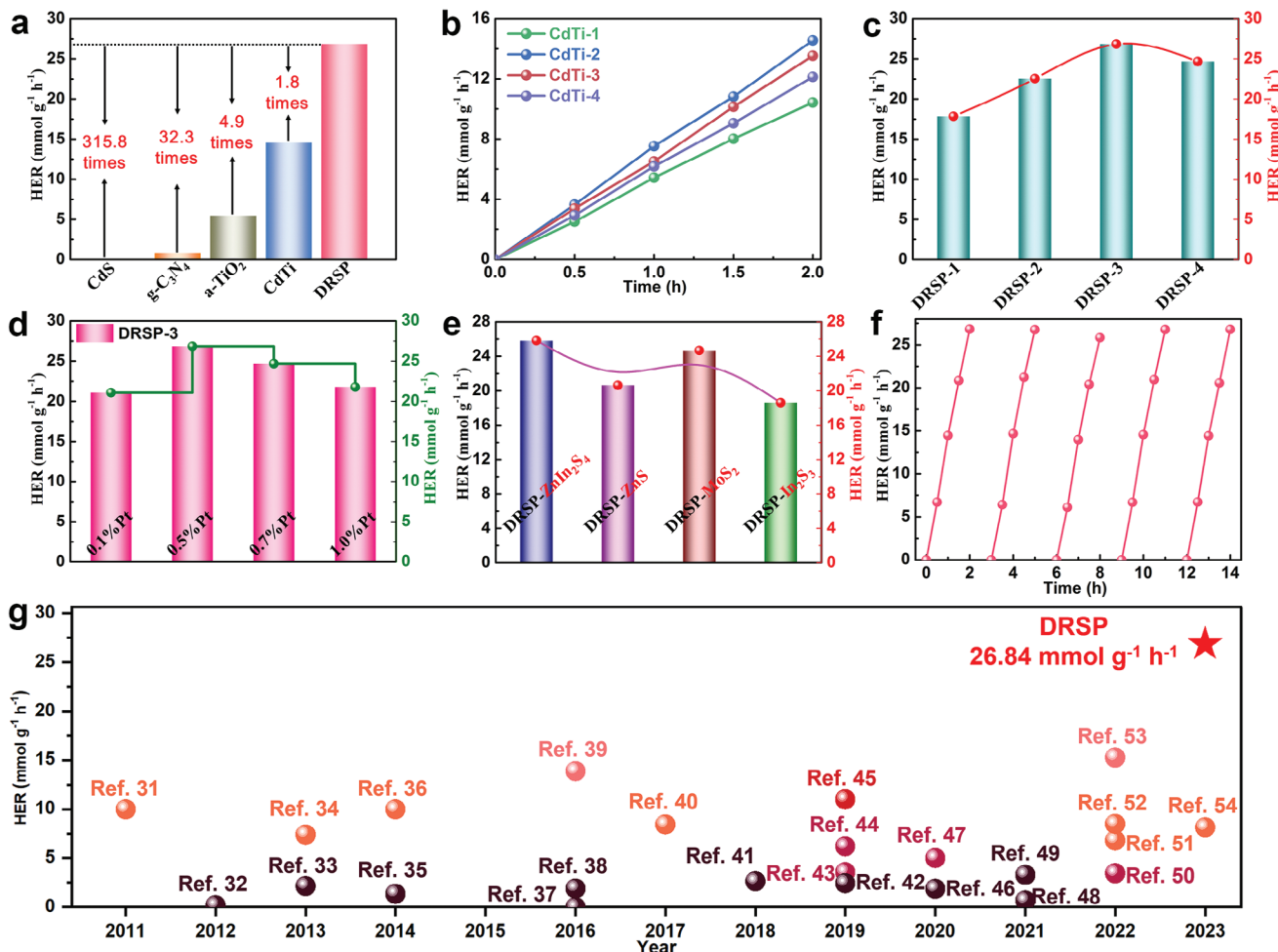
Figure 5. Transient absorption spectra of a,b) CdS, d,e) a-TiO₂, g,h) g-C₃N₄, and j,k) DRSP catalyst. Normalized transient absorption kinetics for c) CdS, f) a-TiO₂, i) g-C₃N₄, and l) DRSP catalyst after 400 nm laser excitation.

carriers' transportation and well maintain the heterojunction with high redox ability.

2.3. Separation And Transportation Of Carriers

The transportation dynamics of double S-scheme DRSP catalyst is investigated by femtosecond transient absorption (fs-TA)

spectroscopy. The excitation wavelength of catalysts is selected at 400 nm based on the corresponding band structures. Pristine CdS shows sharp TA spectra dominated by exciton bleach (XB) peak at 523 nm due to the state-filling effect of band-edge carriers, while anatase TiO₂ demonstrates the broadband absorption within the probe light range of 420–600 nm with an absorption peak maximum at 450 nm (Figure 5a,d). Pristine g-C₃N₄ shows distinct XB absorption with its peak position at 415 nm while



ratio of a-TiO₂ on CdS. The result shows that CdTi-2 exhibits excellent hydrogen evolution performance (Figure 6b). Then, we choose the optimized CdTi-2 binary catalyst to couple with different amounts of g-C₃N₄ and investigate the performance. As shown in Figure 6c, DRSP-3 exhibits a superior photocatalytic hydrogen evolution performance than any other proportion DRSP catalysts.

In order to obtain the best performance, the mass ratio of co-catalyst Pt is also optimized and the result shows that the hydrogen evolution performance reaches the highest when the Pt loading amount is 0.5 wt% (Figure 6d). Excessive loading amount of Pt will cover the active sites of DRSP, thus leading to the decreased photocatalytic hydrogen evolution rate. Meanwhile, the apparent quantum efficiency (AQE) is also tested, which is a key evaluation factor for photocatalytic performance. The photon utilization efficiency of DRSP achieves 40.2% at a wavelength of 365 nm, which is higher than other reported photocatalysts in the literature (Figure S18 Supporting Information). More importantly, in order to confirm our proposed dual reduction site induced by double S-scheme transfer path, we change one reduction type semiconductor (CdS) into several other similar metal sulfides (ZnIn₂S₄, ZnS, MoS₂, and In₂S₃) and investigate the corresponding photocatalytic hydrogen evolution performance. The results show that as-prepared catalysts also have excellent photocatalytic hydrogen evolution performance, further confirming our proposed double S-scheme mechanism (Figure 6e).

The cycling hydrogen evolution performances of DRSP exhibit refreshable photocatalytic activities and XRD patterns, XPS and TEM of DRSP achieved before and after photocatalytic reaction confirm the well-maintained catalyst structure, suggesting that as-prepared DRSP has a superior stability (Figure 6f and Figure S19-22 Supporting Information). To the best of our knowledge, the photocatalytic hydrogen evolution rate of DRSP we obtained is far exceeding that of most reported catalysts (Figure 6g and Figure S23 Supporting Information).^[31–54]

3. Conclusions

In conclusion, we have effectively constructed a double S-scheme structure with CdS nanospheres decorated with anatase TiO₂ nanoparticles coupled by graphitic carbon nitride nanosheets. The constructed double S-scheme transfer mechanism resulted in dual reduction sites, which can optimize the separation and transfer of photogenerated carriers while preserving their reductive potential. As-prepared DRSP catalyst shows an impressive photocatalytic hydrogen evolution rate of 26.84 mmol g⁻¹ h⁻¹ and highest apparent quantum efficiency of 40.2% at the wavelength of 365 nm. The enhancement of photocatalytic performance is induced by a double S-scheme charge transfer route, which can inhibit the undesired recombination of photogenerated charge carriers, enhance spatial carrier transport, and maximize redox capabilities. This work provides an effective method to design other double S-scheme junctions with dual reduction site and presents new insights into designing artificial photosynthetic systems.

Supporting Information

Supporting Information is available from the Wiley Online Library or from the author.

Acknowledgements

This study was supported by the National Natural Science Foundation of China (51872116, 12034002, and 22279044), Jilin Province Science and Technology Development Program (20210301009GX), project for Self-innovation Capability Construction of Jilin Province Development and Reform Commission (2021C026) and the Fundamental Research Funds for the Central Universities, and City University of Hong Kong (CityU 9610577).

Conflict of Interest

The authors declare no conflict of interest.

Data Availability Statement

Research data are not shared.

Keywords

artificial photosynthetic system, double S-scheme, dual reduction site, hydrogen evolution, photocatalyst

Received: September 7, 2023
Revised: October 30, 2023
Published online:

- [1] X. Tao, Y. Zhao, S. Wang, C. Li, R. Li, *Chem. Soc. Rev.* **2022**, *51*, 3561.
- [2] H. Liu, M. Cheng, Y. Liu, J. Wang, G. Zhang, L. Li, L. Du, G. Wang, S. Yang, X. Wang, *Energy Environ. Sci.* **2022**, *15*, 3722.
- [3] X.-B. Li, C.-H. Tung, L.-Z. Wu, *Nat. Rev. Chem.* **2018**, *2*, 160.
- [4] X. Liu, S. Inagaki, J. Gong, *Angew. Chem., Int. Ed.* **2016**, *55*, 14924.
- [5] H. Tan, P. Zhou, M. Liu, Q. Zhang, F. Liu, H. Guo, Y. Zhou, Y. Chen, L. Zeng, L. Gu, Z. Zheng, M. Tong, S. Guo, *Nat Synth* **2023**, *2*, 557.
- [6] H. Li, R. Li, G. Liu, M. Zhai, J. Yu, *Adv. Mater.* **2023**, 2301307.
- [7] Z. Wang, Z. Lin, S. Shen, W. Zhong, S. Cao, *Chin. J. Catal.* **2021**, *42*, 710.
- [8] M. Zhang, Y. Mao, X. Bao, G. Zhai, D. Xiao, D. Liu, P. Wang, H. Cheng, Y. Liu, Z. Zheng, Y. Dai, Y. Fan, Z. Wang, B. Huang, *Angew. Chem., Int. Ed.* **2023**, e202302919.
- [9] H. Zhao, L. Wang, G. Liu, Y. Liu, S. Zhang, L. Wang, X. Zheng, L. Zhou, J. Gao, J. Shi, Y. Jiang, *ACS Catal.* **2023**, *13*, 6619.
- [10] Q. Chen, X. Chen, Q. Jiang, Z. Zheng, Z. Song, Z. Zhao, Z. Xie, Q. Kuang, *Appl. Catal. B* **2021**, *297*, 120394.
- [11] H. Li, C. Cheng, Z. Yang, J. Wei, *Nat. Commun.* **2022**, *13*, 6466.
- [12] P. Zhou, I. A. Navid, Y. Ma, Y. Xiao, P. Wang, Z. Ye, B. Zhou, K. Sun, Z. Mi, *Nature* **2023**, *613*, 66.
- [13] W. Zhang, A. R. Mohamed, W.-J. Ong, *Angew. Chem., Int. Ed.* **2020**, *59*, 22894.
- [14] Y. Wang, X. Shang, J. Shen, Z. Zhang, D. Wang, J. Lin, J. C. S. Wu, X. Fu, X. Wang, C. Li, *Nat. Commun.* **2020**, *11*, 3043.
- [15] M. Zhang, M. Lu, Z.-L. Lang, J. Liu, M. Liu, J.-N. Chang, L.-Y. Li, L.-J. Shang, M. Wang, S.-L. Li, Y.-Q. Lan, *Angew. Chem., Int. Ed.* **2020**, *59*, 6500.
- [16] R. Shen, G. Liang, L. Hao, P. Zhang, X. Li, *Adv. Mater.* **2023**, 2303649.
- [17] L. Zhang, J. Zhang, H. Yu, J. Yu, *Adv. Mater.* **2022**, *34*, 2107668.
- [18] X. Ruan, C. Huang, H. Cheng, Z. Zhang, Y. Cui, Z. Li, T. Xie, K. Ba, H. Zhang, L. Zhang, X. Zhao, J. Leng, S. Jin, W. Zhang, W. Zheng, S. K. Ravi, Z. Jiang, X. Cui, J. Yu, *Adv. Mater.* **2023**, *35*, 2209141.
- [19] Q. Xu, L. Zhang, B. Cheng, J. Fan, J. Yu, *Chem* **2020**, *6*, 1543.

- [20] Z. Gao, Y. Jian, S. Yang, Q. Xie, C. J. Ross Mcfadzean, B. Wei, J. Tang, J. Yuan, C. Pan, G. Yu, *Angew. Chem., Int. Ed.* **2023**, *62*, e202304173.
- [21] Q. Xu, S. Wageh, A. A. Al-Ghamdi, X. Li, *J. Mater. Sci. Technol.* **2022**, *124*, 171.
- [22] C. Feng, J. Rong, Y. Zhang, X. Zheng, X. Li, S. Xu, Z. Li, *Appl. Catal. B* **2023**, *337*, 123005.
- [23] Y. Zhang, J. Di, X. Zhu, M. Ji, C. Chen, Y. Liu, L. Li, T. Wei, H. Li, J. Xia, *Appl. Catal. B* **2023**, *323*, 122148.
- [24] F. Xu, K. Meng, B. Cheng, S. Wang, J. Xu, J. Yu, *Nat. Commun.* **2020**, *11*, 4613.
- [25] X. Luan, Z. Yu, J. Zi, F. Gao, Z. Lian, *Adv. Funct. Mater.* **2023**, *2304259*.
- [26] Y. Zhang, Y. Li, X. Xin, Y. Wang, P. Guo, R. Wang, B. Wang, W. Huang, A. J. Sobrido, X. Li, *Nat. Energy* **2023**, *8*, 504.
- [27] G. Sun, Z. Tai, F. Li, Q. Ye, T. Wang, Z. Fang, L. Jia, W. Liu, H. Wang, *Small* **2023**, *19*, 2207758.
- [28] R. Shi, H.-F. Ye, F. Liang, Z. Wang, K. Li, Y. Weng, Z. Lin, W.-F. Fu, C.-M. Che, Y. Chen, *Adv. Mater.* **2018**, *30*, 1705941.
- [29] X. Ruan, X. Cui, G. Jia, J. Wu, J. Zhao, D. J. Singh, Y. Liu, H. Zhang, L. Zhang, W. Zheng, *Chem. Eng. J.* **2022**, *428*, 132579.
- [30] X. Ruan, X. Cui, Y. Cui, X. Fan, Z. Li, T. Xie, K. Ba, G. Jia, H. Zhang, L. Zhang, W. Zhang, X. Zhao, J. Leng, S. Jin, D. J. Singh, W. Zheng, W. Zheng, *Adv. Energy Mater.* **2022**, *12*, 2200298.
- [31] X. Chen, L. Liu, P. Y. Yu, S. S. Mao, *Science* **2011**, *331*, 746.
- [32] F. Zuo, K. Bozhilov, R. J. Dillon, L. Wang, P. Smith, X. Zhao, C. Bardeen, P. Feng, *Angew. Chem., Int. Ed.* **2012**, *51*, 6223.
- [33] Z. Wang, C. Yang, T. Lin, H. Yin, P. Chen, D. Wan, F. Xu, F. Huang, J. Lin, X. Xie, M. Jiang, *Adv. Funct. Mater.* **2013**, *23*, 5444.
- [34] Z. Wang, C. Yang, T. Lin, H. Yin, P. Chen, D. Wan, F. Xu, F. Huang, J. Lin, X. Xie, M. Jiang, *Energy Environ. Sci.* **2013**, *6*, 3007.
- [35] W. Zhou, W. Li, J.-Q. Wang, Y. Qu, Y. Yang, Y. Xie, K. Zhang, L. Wang, H. Fu, D. Zhao, *J. Am. Chem. Soc.* **2014**, *136*, 9280.
- [36] T. Lin, C. Yang, Z. Wang, H. Yin, X. Lü, F. Huang, J. Lin, X. Xie, M. Jiang, *Energy Environ. Sci.* **2014**, *7*, 967.
- [37] B. Wu, D. Liu, S. Mubeen, T. T. Chuong, M. Moskovits, G. D. Stucky, *J. Am. Chem. Soc.* **2016**, *138*, 1114.
- [38] S. F. Kou, W. Ye, X. Guo, X. F. Xu, H. Y. Sun, J. Yang, *RSC Adv.* **2016**, *6*, 39144.
- [39] K. Zhang, L. Wang, J. K. Kim, M. Ma, G. Veerappan, C.-L. Lee, K.-J. Kong, H. Lee, J. H. Park, *Energy Environ. Sci.* **2016**, *9*, 499.
- [40] Y. Sui, S. Liu, T. Li, Q. Liu, T. Jiang, Y. Guo, J.-L. Luo, *J. Catal.* **2017**, *353*, 250.
- [41] S. Atta, A. M. Pennington, F. E. Celik, L. Fabris, *Chem* **2018**, *4*, 2140.
- [42] W. Wang, S. Zhu, Y. Cao, Y. Tao, X. Li, D. Pan, D. L. Phillips, D. Zhang, M. Chen, G. Li, H. Li, *Adv. Funct. Mater.* **2019**, *29*, 1901958.
- [43] H. Xiong, L. Wu, Y. Liu, T. Gao, K. Li, Y. Long, R. Zhang, L. Zhang, Z.-A. Qiao, Q. Huo, X. Ge, S. Song, H. Zhang, *Adv. Energy Mater.* **2019**, *9*, 1901634.
- [44] X. Shi, S. Kim, M. Fujitsuka, T. Majima, *Appl. Catal. B* **2019**, *254*, 594.
- [45] Y. Li, Y.-K. Peng, L. Hu, J. Zheng, D. Prabhakaran, S. Wu, T. J. Puchtler, M. Li, K.-Y. Wong, R. A. Taylor, S. C. E. Tsang, *Nat. Commun.* **2019**, *10*, 4421.
- [46] M. Xiao, L. Zhang, B. Luo, M. Lyu, Z. Wang, H. Huang, S. Wang, A. Du, L. Wang, *Angew. Chem., Int. Ed.* **2020**, *59*, 7230.
- [47] B. Yan, D. Liu, X. Feng, M. Shao, Y. Zhang, *Adv. Funct. Mater.* **2020**, *30*, 2003007.
- [48] S. Li, Y. H. Ng, R. Zhu, S. Lv, C. Wu, Y. Liu, L. Jing, J. Deng, H. Dai, *Appl. Catal. B* **2021**, *297*, 120412.
- [49] D. Gao, W. Zhong, Y. Liu, H. Yu, J. Fan, *Appl. Catal. B* **2021**, *290*, 120057.
- [50] L. Wang, G. Tang, S. Liu, H. Dong, Q. Liu, J. Sun, H. Tang, *Chem. Eng. J.* **2022**, *428*, 131338.
- [51] G. Jia, Y. Wang, X. Cui, H. Zhang, J. Zhao, L. H. Li, L. Gu, Q. Zhang, L. Zheng, J. Wu, Q. Wu, D. J. Singh, W. Li, L. Zhang, W. Zheng, *Matter* **2022**, *5*, 206.
- [52] M. Torras, P. Molet, L. Soler, J. Llorca, A. Roig, A. Mihi, *Adv. Energy Mater.* **2022**, *12*, 2103733.
- [53] H. Zeng, Z. Li, G. Li, X. Cui, M. Jin, T. Xie, L. Liu, M. Jiang, X. Zhong, Y. Zhang, H. Zhang, K. Ba, Z. Yan, Y. Wang, S. Song, K. Huang, S. Feng, *Adv. Energy Mater.* **2022**, *12*, 2102765.
- [54] H. S. Moon, K.-C. Hsiao, M.-C. Wu, Y. Yun, Y.-J. Hsu, K. Yong, *Adv. Mater.* **2023**, *35*, 2200172.